Evolution of Shock-Induced Orientation-Dependent Metastable States in Crystalline Aluminum

Mikalai M. Budzevich,[1] Vasily V. Zhakhovsky,[1,*] Carter T. White,[2] and Ivan I. Oleynik[1,†]

[1]*Department of Physics, University of South Florida, Tampa, Florida 33620, USA*

[2]*Naval Research Laboratory, Washington, DC 20375, USA*

(Received 2 February 2012; published 19 September 2012)

The evolution of orientation-dependent metastable states during shock-induced solid-liquid phase transitions in crystalline Al is followed using moving window molecular dynamics simulations. The orientation-dependent transition pathways towards an orientation-independent final state Hugoniot include both ''cold melting'' followed by recrystallization in [110]- and [111]-oriented shock waves and crystal overheating followed by melting in [100] shock waves. The orientation-dependent dynamics take place within a zone that can extend up to hundreds of nanometers behind the shock front.

DOI: 10.1103/PhysRevLett.109.125505 PACS numbers: 62.50.Ef, 02.70.Ns, 64.70.dg, 64.70.dj

Anisotropic mechanical properties are characteristic of crystalline solids exemplified by variation of their elastic constants in different crystallographic directions [1]. Therefore, such an orientation-dependent mechanical response might also be expected upon uniaxial compression of single crystals by shock waves [2,3]. In fact, molecular dynamics (MD) simulations have predicted an orientation dependence in the shock-induced melting transition in face-centered cubic (fcc) metal single crystals [4–7]. For example, the Cu crystal was overheated without melting by as much as 20% above the equilibrium melting line for shock compression in the [100] direction but exhibited a so-called ''cold melting'' in the [110] and [111] directions that occurred at temperatures about 7–8% below the melting line [6]. A similar behavior was found in Pt leading to orientation-dependent solid-liquid Hugoniots [7]. For such intense shock waves, this behavior is puzzling, as only an orientation-independent Hugoniot was observed in experiments on single Cu crystals shocked along the [100], [110], and [111] directions at somewhat lower shock-wave strengths [8].

We provide a solution to this conundrum by following the evolution of orientation-dependent metastable states during shock-induced solid-liquid phase transitions along the [100], [110], and [111] directions in single crystal Al using a novel moving window molecular dynamics (MWMD) technique [9,10]. Our results show that distinctly different transition pathways for shock compression along different directions converge towards an orientation-independent $T - P$ Hugoniot, even for single crystals. However, they also indicate that orientation effects can persist over large enough distances in the after-shock flow to be probed experimentally.

The dynamics of solid-liquid phase transitions in a perfect fcc Al crystal under shock loading were investigated using samples in which the x axis of the MWMD box was oriented along the [100], [110], and [111] crystallographic directions, with periodic boundary conditions imposed along the lateral y and z directions. Typical samples contained $\sim 4 \times 10^6$ atoms and had dimensions $L_x = 200$–400 nm and $L_y = L_z = 12$ nm. The interatomic interactions in Al were described by an embedded atom method potential specifically developed to simulate conditions of extreme stress [10,11] and validated [10] (see Supplemental Material [12]) against experimental data [13] encompassing the elastic, plastic, and melting regimes of shock-wave response. Using this potential, a series of MWMD simulations was performed for steady shock-wave speeds u_s in the interval 8.5–15 km/s to include the melting regime.

A good probe of atomic order is the radial distribution function (RDF), which can detect correlations far beyond the first coordination shell and hence aid in determining if the system is liquid or solid. For a shocked material undergoing a phase transformation in the after-shock flow, the spherical RDF is not applicable, however, because the material properties change along the flow direction (x axis in our simulations). Rather, the in-plane RDF [14] is used because at the steady-state conditions of our simulations the averaged system properties do not change at a constant distance behind the shock front. A cross section of the MW simulation cell was used to evaluate this function, with atoms displaced along x by ± 0.05 nm from the cross section counted as part of the plane.

The local order parameter Q_6 [15] was used to construct color images of the rich structure that can occur during melting and solidification. Q_6 was first evaluated for a given atom by including only that atom and its nearest neighbors [16] defined by Voronoi decomposition. These atomic-centered values were then averaged over the several hundred atoms contained in a small rectangular box extending across the simulation cell [long axis parallel to the z axis of the cell and passing through the point (x, y)] to obtain $\bar{Q}_6(x, y)$ used in the color map. Steady profiles of $\bar{Q}_6(x)$, denoted by $\bar{\bar{Q}}_6(x)$, and $T(x)$ were obtained by temporal and spatial averaging of data collected 100 times over ~ 15 ps from a thin lateral slice of the simulation cell located a distance x from the shock front and containing ~ 5300 atoms.

To illustrate the major features of material evolution from single crystal through cold melt to polycrystalline solid in both the [110] and [111] directions, consider the case of a shock wave propagating in the [110] direction with speed $u_s = 10.07$ km/s corresponding to a particle velocity $u_p = 3.420$ km/s. See Fig. 1. Initially, the shocked material experiences high strain rate deformations and very large shear stress buildup, which is later released by shear-induced mechanical melting accompanied by a rapid rise in $T(x)$. This ultrafast mechanical melting, completed within a ~1–2 nm thick shock front, results in a state at a temperature 984 K lower than the simulated equilibrium melting temperature for Al at the given shock pressure and hence is termed "cold melting."

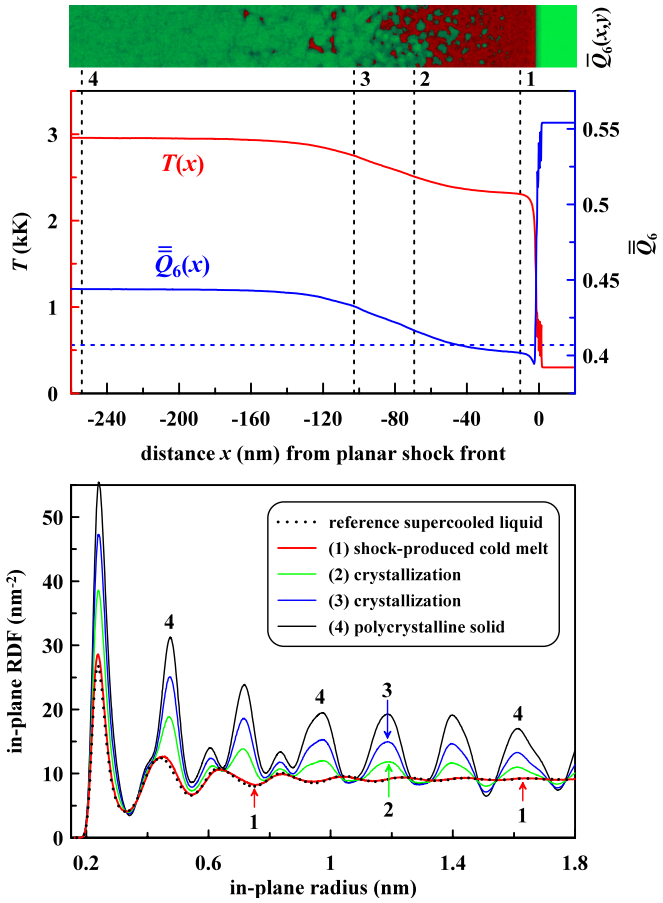

FIG. 1 (color online). Cold melting followed by recrystallization produced by a [110] shock wave with $u_s = 10.07$ km/s. Top pane: Snapshot of color map of $\bar{\bar{Q}}_6(x, y)$. Green (red) regions of the map correspond to the solid (cold-melted) phase. Middle pane: Steady-state profiles of $\bar{\bar{Q}}_6(x)$ and temperature $T(x)$. Increase of $\bar{\bar{Q}}_6(x)$ and $T(x)$ in the after-shock flow corresponds to recrystallization of the supercooled melt. Horizontal dashed line indicates boundary separating red (liquid) from green (solid) color scales in the top pane. Bottom pane: In-plane RDF at positions behind the shock front specified by the vertical dashed lines in the middle pane. Also shown in this pane is the in-plane RDF for the reference supercooled state described in the text.

High strain rate deformations and large shear stress buildup are also present during elastic-plastic transformations caused by a strong shock wave with an intensity somewhat below the onset of cold melting. In that case, however, the large shear stress buildup at the shock front is released by the production of point and extended defects, including dislocations, and the material does not melt. In contrast, the metastable cold-melted state has a structure measured by the in-plane RDF (see Fig. 1) and self-diffusion coefficient (see Supplemental Material [12]) that are practically the same as a metastable supercooled liquid reference state at the same temperature and density as the liquid state present at the end of cold melting.

The reference supercooled state was formed by rapidly quenching an equilibrium melt at the same density as the cold-melted state in a periodically repeated simulation cell to the temperature of the shock-induced cold-melted state. When followed using NVE MD (constant number of particles, volume, and energy MD), this supercooled melted state persisted for ~53 ps at the quench temperature, whereupon a critical nucleus formed and recrystallization began accompanied by an increase in T.

The cold-melted state predominates to ~35 nm behind the shock front, largely solidifies over the next ~80 nm, and then gradually approaches a polycrystalline solid, as reflected by the changing slopes of $T(x)$ and $\bar{\bar{Q}}_6(x)$ in Fig. 1. Because the shock front moves at 10.07 km/s but the particle flow velocity behind it is 3.42 km/s, a thin slice of material recedes from the front at 6.65 km/s and hence resides in the cold-melted region for ~5 ps before taking ~20 ps to solidify. Although the change in T accompanying solidification of the cold-melted and reference supercooled states is the same, the shorter time the slice resides in the cold-melted state suggests that a few crystallites survive the process of cold melting, later to serve as nucleation centers during solidification.

Accompanying the transition from cold-melted to solid state, the in-plane RDF evolves from one corresponding to a liquid to one exhibiting many peaks. This could not have occurred if the cold-melted state had been a solid rather than a liquid. Indeed, even if the cold-melted state had been an amorphous solid at the glass transition temperature T_g, the required atomic rearrangements would have taken at least 10^3 s plus or minus an order of magnitude or two [17]. However, this time is at least 11 orders of magnitude slower than the ~20 ps required for resolidification. Furthermore, because the temperature of the cold-melted state must then be above T_g and the final solid is at the same pressure as the melt but at a higher temperature (see Fig. 2), the final solid is not a glass. This is not surprising, as pure metals are not known to form glasses except perhaps via vapor deposition of thin films on ultracold substrates [18]. As the final solid state is not a glass and not a pure crystal, it is a polycrystalline solid.

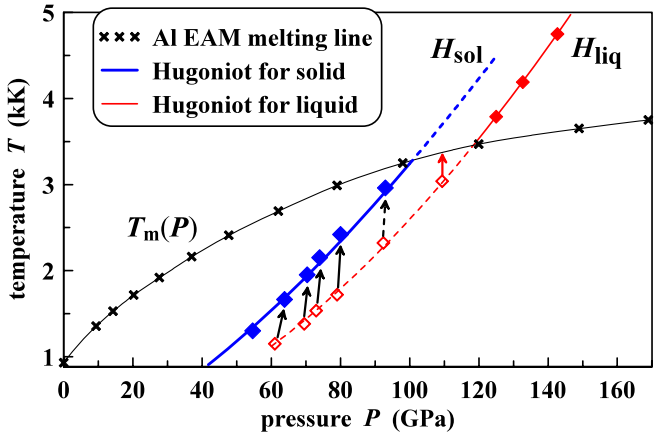

FIG. 2 (color online). Simulated solid H_{sol} and liquid H_{liq} branches of the $T - P$ Hugoniot for shock compression of Al in the [110] direction together with the theoretical melting line $T_m(P)$. The thinner red dashed line with open diamonds corresponds to initial metastable supercooled states right behind the shock front; the thicker blue solid line with solid diamonds corresponds to equilibrium recrystallized states far behind the shock front.

Fast cold melting followed by slower recrystallization was observed in the after-shock flow of Al for both the [110] and [111] directions within the range of shock-wave velocities $u_s = 9.1$–10.8 km/s. For a given u_s, two (P, T) points were determined from the pressure and the temperature profiles: (P_1, T_1) for the supercooled molten state of Al right behind the shock front and (P_2, T_2) for the solid far behind the shock front. By plotting points 1 and 2 for each u_s, $T - P$ liquid and solid branches of the Hugoniot were obtained as shown in Fig. 2 for [110] shock-compressed Al, where the red dashed (blue solid) line with open (solid) diamonds corresponds to initial (final) supercooled (polycrystalline) states right (far) behind the shock front. Figure 2 also includes the theoretical melting line $T_m(P)$ obtained by the phase coexistence method.

In the [110] direction, the regime of cold melting followed by recrystallization was observed in the range of shock pressures 61–100 GPa. The black vectors in Fig. 2 connecting the open and solid diamonds indicate trajectories from the supercooled melt to the final recrystallized material in the after-shock flow. The first solid black vector corresponds to a specific case $u_s = 9.0$ km/s and involves both the initial supercooled state (61 GPa, 1150 K) and the recrystallized final state 63.8 GPa, 1663 K. The theoretical equilibrium melting temperature at 61 GPa was $T_m = 2670$ K; therefore, the initial cold melting occurred at a temperature lower than T_m by 1520 K. The dashed vector corresponds to the case $u_s = 10.07$ km/s discussed above and shown in Fig. 1. The blue solid diamond at ≈ 54 GPa and the red solid diamonds above 123 GPa correspond to plastic and melted states below and above the states below and above the cold melting followed by recrystallization regime.

The red vector, starting from the supercooled state (109.4 GPa, 3038 K) and ending at the equilibrium melting line shown in Fig. 2, corresponds to partial recrystallization at $u_s = 10.63$ km/s. The time it takes the supercooled melt to reach the final state rapidly increases, as the difference between the temperature of the supercooled state T_1 and the equilibrium melting temperature T_m at a given shock pressure P decreases. Therefore, for $u_s = 10.63$ km/s, which has an initial state close to the equilibrium melting line, the final equilibrium state was impossible to achieve within a 600 nm long MWMD box, the largest used in our simulations.

Having underlined the importance of shear stresses in shock-induced solid-liquid phase transitions, it is natural to expect a different mechanism of shock-induced melting in the [100] crystallographic direction based on the well-known fact that for fcc crystals the [100] shear stresses are much smaller than those for the [110] and [111] directions under the same uniaxial compressive strain. Indeed, a substantial overheating followed by melting, rather than cold melting followed by recrystallization, was observed upon shock compression of Al in the [100] direction within the interval of shock velocities $u_s = 10.8$–11.05 km/s. Therefore, uniaxial shock compression along the [100] direction resulted in overheating of Al above the equilibrium melting line right behind the shock front. Such an overheated metastable state subsequently underwent a melting transition in the after-shock flow.

An example of overheating followed by melting produced by a [100] shock wave with $u_s = 10.85$ km/s (corresponding to a particle velocity $u_p = 4.019$ km/s) is shown in Fig. 3. The overheated solid predominates for about 15 nm right behind the shock front, largely melts over the next ~40 nm, and then gradually approaches an equilibrium liquid over the next ~240 nm, as reflected by the changing slopes of $T(x)$ and $\bar{\bar{Q}}(x)$ in Fig. 3. Because a thin slice of the material recedes from the front at a speed of 6.83 km/s, it only resides in the overheated region for ~2 ps before taking ~40 ps to arrive at the completely melted final equilibrium state accompanied by a reduction in $T(x)$ from 3970 K to 3420 K.

The in-plane RDF for the shock-induced overheated metastable state is practically identical to that of an overheated metastable reference state. The reference state was formed by uniaxially compressing an Al crystal along the [100] direction to the same density as the shock-induced overheated state, heating it to the temperature of the shock-induced overheated state and then using NVE MD to follow its evolution until it melted in ~20 ps. The agreement between the two RDFs indicates that the shock-induced overheated state is largely crystalline and, hence, does not have sufficient time to undergo significant plastic deformation prior to melting. Nevertheless, the narrow extent of the shock-induced overheated state suggests that the shock wave does first

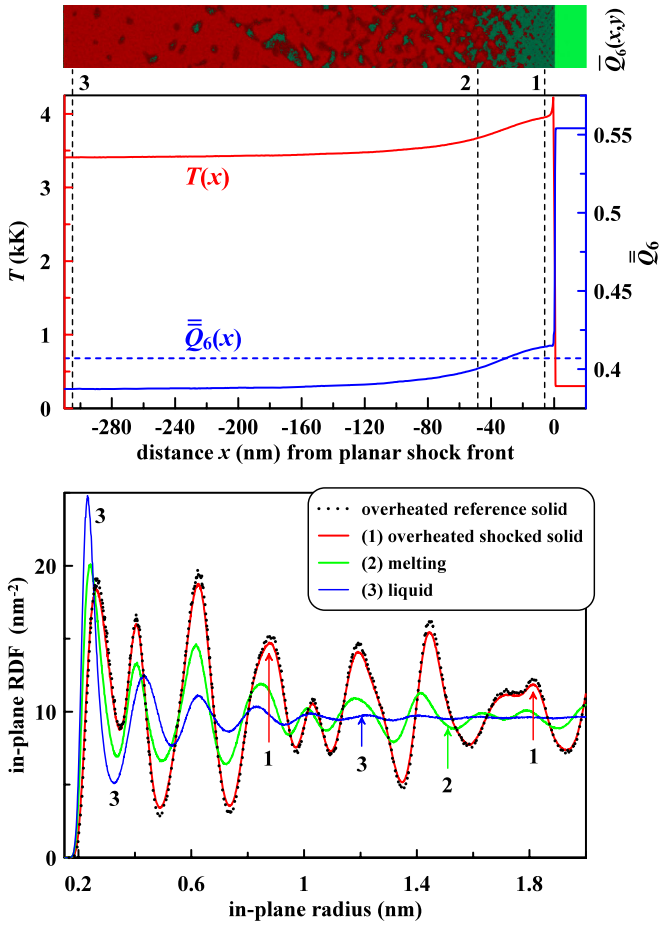

FIG. 3 (color online). Overheating of the Al crystal followed by melting produced by a [100] shock wave with $u_s = 10.85$ km/s. Top pane: Snapshot of color map of $\bar{\bar{Q}}_6(x, y)$. Green (red) regions on the map correspond to the solid (liquid) phase. Middle pane: Steady-state profiles of $\bar{\bar{Q}}_6(x, y)$ and temperature $T(x)$. Decrease of $\bar{\bar{Q}}(x, y)$ and $T(x)$ in after-shock flow corresponds to melting of the overheated crystal. Horizontal dashed line indicates boundary separating red (liquid) from green (solid) color scales used in the top pane. Bottom pane: In-plane RDF at positions behind shock front specified by vertical dashed lines in middle pane. Also shown is the reference overheated state described in the text.

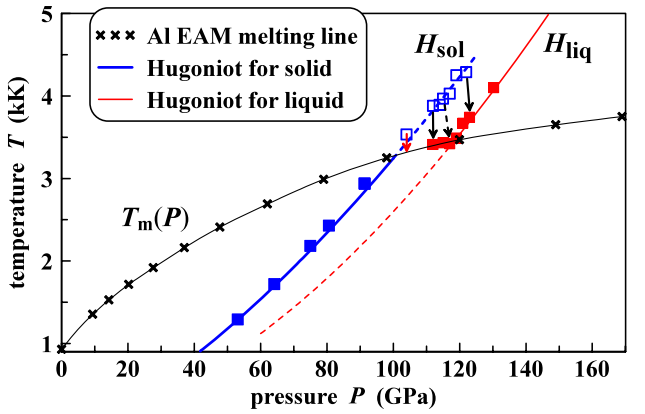

FIG. 4 (color online). Simulated solid H_{sol} and liquid H_{liq} branches of the $T - P$ Hugoniot for shock compression of Al in the [100] direction together with the theoretical melting line $T_m(P)$. The thicker blue dashed line with open squares corresponds to initial metastable overheated states right behind the shock front; the thinner red solid line with solid squares corresponds to equilibrium melted states far behind the shock front.

introduce some residual disordering that serves to promote melting.

The solid and liquid branches of the $T - P$ Hugoniot for shock compression in the [100] direction are shown in Fig. 4. Because of the substantially smaller shear stresses along [100] direction ($\lesssim 1.9$ GPa), the shocked material remains solid up to the onset of equilibrium melting at 101 GPa. See solid blue squares on solid blue line in Fig. 4. The overheated states right behind the shock front appeared in the interval of shock pressures between 101 and 122 GPa (see open blue squares on dashed blue line in Fig. 4), with final states at the equilibrium melting line for shocks with pressures between 101 and 119 GPa The black vectors connecting open and solid squares indicate trajectories from the overheated crystal to equilibrium partially melted or fully melted states in the after-shock flow. The dashed black vector corresponds to the case $u_s = 10.85$ km/s, shown in Fig. 3.

In contrast to the [110] and [111] compressions, we were able to observe partial solid-liquid phase transitions along the [100] direction to their completion for cases having final equilibrium states lying on the melting line $T_m(P)$. The only exception is indicated by a small solid red vector in Fig. 4, close to the intersection of the solid Hugoniot and the melting line. The maximum overheating temperature observed in our simulations was only 583 K above the corresponding melting point $T_m(P)$. Above 123 GPa the [100] crystal underwent ultrafast equilibrium melting within a very narrow zone behind the shock front.

Despite very different pathways, the final solid and liquid states all converge to the same Hugoniot, consisting of both solid and liquid branches connected by a segment of the equilibrium melting line. The solid and liquid Hugoniot lines H_{sol} and H_{liq} in both Figs. 2 and 4 are fits of combined [100] and [110] sets of equilibrium and metastable (P, T) points. The metastable states in both cases (open red diamonds for the [110] direction and open blue squares for the [100] direction) lie on metastable branches of H_{sol} and H_{liq} extrapolated beyond the corresponding orientation-independent Hugoniots.

Although all directions converge to the same Hugoniot, this need not imply that the microstructures of the final states are identical. In particular, cold melting followed by recrystallization produced by [110] and [111] shock waves yield polycrystalline solids that are more disordered than the corresponding solid produced by a [100] shock wave resulting in practically the same point on the final Hugoniot. These orientation effects should persist for many microns in the

shock after flow making them experimentally accessible using the novel capabilities of dynamical X-ray scattering [19–21].

The work at USF and NRL was supported by ONR and NRL. The work at USF was also supported by the NSF. Simulations were performed using the NSF TeraGrid facilities, the USF Research Computing Cluster, and the computational facilities of the Materials Simulation Laboratory at USF.

*vasily@usf.edu

†oleynik@usf.edu

[1] C. Kittel, *Introduction to Solid State Physics* (Wiley, New York, 2005), 8th ed.

[2] T. C. Germann, B. L. Holian, P. S. Lomdahl, and R. Ravelo, Phys. Rev. Lett. **84**, 5351 (2000).

[3] E. M. Bringa, J. U. Cazamias, P. Erhart, J. Stölken, N. Tanushev, B. D. Wirth, R. E. Rudd, and M. J. Caturla, J. Appl. Phys. **96**, 3793 (2004).

[4] R. Ravelo, B. L. Holian, T. C. Germann, and P. Lomdahl, AIP Conf. Proc. **845**, 270 (2006).

[5] K. Kadau, T. C. Germann, P. Lomdahl, and B. L. Holian, AIP Conf. Proc. **845**, 236 (2006).

[6] Q. An, S.-N. Luo, L.-B. Han, L. Zheng, and O. Tschauner, J. Phys. Condens. Matter **20**, 095220 (2008).

[7] Z.-L. Liu, J.-H. Yang, Z.-G. Zhao, L.-C. Cai, and F.-Q. Jing, Phys. Lett. A **374**, 1579 (2010).

[8] R. Chau, J. Stölken, P. Asoka-Kumar, M. Kumar, and N. C. Holmes, J. Appl. Phys. **107**, 023506 (2010).

[9] V. V. Zhakhovskii, K. Nishihara, and S. I. Anisimov, JETP Lett. **66**, 99 (1997).

[10] V. V. Zhakhovsky, M. M. Budzevich, N. A. Inogamov, I. I. Oleynik, and C. T. White, Phys. Rev. Lett. **107**, 135502 (2011).

[11] V. V. Zhakhovskii, N. A. Inogamov, Y. V. Petrov, S. I. Ashitkov, and K. Nishihara, Appl. Surf. Sci. **255**, 9592 (2009).

[12] See Supplemental Material at http://link.aps.org/supplemental/10.1103/PhysRevLett.109.125505 for a comparison of shock-wave velocity vs particle velocity Hugoniot predicted by the Al potential to experimental data including the melting regime and for a plot of the mean-squared displacement of particles in the after-shock flow, together with results for the self-diffusion coefficient for the cold-melted and reference supercooled liquids.

[13] Shock wave database: http://teos.ficp.ac.ru/rusbank/.

[14] V. Sorkin, E. Polturak, and J. Adler, Phys. Rev. B **68**, 174103 (2003).

[15] P. J. Steinhardt, D. R. Nelson, and M. Ronchetti, Phys. Rev. B **28**, 784 (1983).

[16] B. A. Klumov, Phys. Usp. **53**, 1053 (2010).

[17] R. Zallen, *The Physics of Amorphous Solids* (Wiley, New York, 1983).

[18] N. P. Kovalenko, Y. P. Krasny, and U. Krey, *Physics of Amorphous Metals* (Wiley, New York, 2001).

[19] D. H. Kalantar *et al.*, Phys. Rev. Lett. **95**, 075502 (2005).

[20] K. Rosolankova, J. S. Wark, E. M. Bringa, and J. Hawreliak, J. Phys. Condens. Matter **18**, 6749 (2006).

[21] A. M. Lindenberg *et al.*, Phys. Rev. Lett. **100**, 135502 (2008).